

FASHI: A search for extragalactic OH megamasers with FASTCHUAN-PENG ZHANG,^{1,2} CHENG CHENG,³ MING ZHU,^{1,2} JIN-LONG XU,^{1,2} AND PENG JIANG^{1,2}¹*National Astronomical Observatories, Chinese Academy of Sciences, Beijing 100101, China*²*Guizhou Radio Astronomical Observatory, Guizhou University, Guiyang 550000, China*³*Chinese Academy of Sciences South America Center for Astronomy, National Astronomical Observatories, CAS, Beijing 100101, China*

ABSTRACT

The **F**AST **A**ll **S**ky **H**I survey (FASHI) is broader in frequency band and sky volume, and deeper in detection sensitivity than the Arecibo Legacy Fast ALFA survey (ALFALFA). To efficiently expand the sample of OH megamasers (OHMs), whose strongest line has a rest frequency of 1667.35903 MHz, we directly matched the IRAS Point Source Catalog Redshift (PSCz) catalog with the corresponding FASHI data cube. From 145 PSCz sources already covered by FASHI, we obtained 27 OHMs with a detection rate of 18.6%, including 9 previously known and 18 new ones, within a redshift range of $0.14314 \lesssim z_{\text{OH}} \lesssim 0.27656$. We also measured the hyperfine ratio of nine OHMs between the 1667 and 1665 MHz lines. The ratio ranges from 1.32 to 15.22, with an average of $R_{1667:1665} = 4.74$. In a fit to the L_{OH} vs. L_{FIR} relation, we have $\log L_{\text{OH}} = (1.57 \pm 0.10)\log L_{\text{FIR}} - (15.80 \pm 1.19)$, which is almost the same as derived from previous observations. As expected, since the OHM sample was selected by cross-correlation with the IRAS-selected PSCz, our detected OHMs are [ultra]luminous infrared galaxies ([U]LIRGs). However, not all [U]LIRGs have detectable OH emission, suggesting that the OH emission may be triggered within a specific stage of the merger or can only be seen in specific orientations. In general, FAST, with its 19-beam array and UWB receiver, will be a powerful tool for observing more OHMs and unraveling their mystery in the future.

Keywords: Radio telescopes (1360), Megamasers (1023), Hydroxyl masers (771), Redshift surveys (1378), Radio sources (1358)

1. INTRODUCTION

OH megamasers (OHMs) at rest frequencies of 1667 and 1665 MHz in extragalactic systems are valuable indicators of galaxy interactions. These megamasers are thought to originate from the starburst nuclei of merging gas-rich galaxy systems, based on both high-resolution interferometer observations (Lo 2005) and statistical analysis of luminosity functions (Darling & Giovanelli 2002, 2006; Giovanelli & Haynes 2015). OHMs thus offer a distinctive approach to measuring the occurrence of gas-rich galaxy mergers at specific evolutionary stages (Lo 2005). The masing emission or absorption lines are usually broad, with line widths up to 10^3 km s^{-1} , and exhibit an implied isotropic luminosity in the range of $10 - 10^4 L_{\odot}$ (Darling & Giovanelli 2002). OHMs are connected to high-density molecular gas ($n(\text{H}_2) \sim 10^4 \text{ cm}^{-3}$) and strong far-infrared radi-

ation. They can offer potential insights into extreme star formation and galactic evolution, particularly high-redshift OHMs (Darling 2007; Lockett & Elitzur 2008; Roberts et al. 2021; Glowacki et al. 2022; Jarvis et al. 2023). Therefore, investigating OHMs is a meaningful pursuit.

As of now, approximately 136 OHMs have been discovered, for instance, in studies of Darling & Giovanelli (2002); Willett (2012); Haynes et al. (2018); Suess et al. (2016); Hess et al. (2021); Roberts et al. (2021); Glowacki et al. (2022); Jarvis et al. (2023). Searches with the Arecibo telescope represent the most successful tracking or single-point observation to date, detecting approximately 17% of OHMs (Darling & Giovanelli 2000). All OHMs known to date are exclusively associated with [ultra]luminous infrared galaxies ([U]LIRGs), defined as having far-infrared luminosities $\gtrsim 10^{11} L_{\odot}$ and $L_{\text{FIR}} \gtrsim 10^{12} L_{\odot}$, respectively (Baan 1991). However, only about 20% of [U]LIRGs are detected with OHM emission, as shown by studies conducted by Baan (1991); Baan et al. (1992); Darling & Giovanelli (2000, 2001, 2002). The production of OHMs may be a tran-

sient phenomenon in the evolution of a galaxy, from starburst nucleus to an AGN (Wiggins et al. 2016), or may be subject to beaming and orientation effects, as suggested in Darling (2007).

The Five-hundred-meter Aperture Spherical radio Telescope (FAST) All Sky HI survey (FASHI) aims to cover the entire sky visible to FAST, between declinations of -14° and $+66^\circ$, within a frequency range of 1.0 – 1.5 GHz (Nan et al. 2011; Jiang et al. 2019, 2020). The survey currently has a typical map rms of ~ 0.76 mJy beam $^{-1}$ and a spectral detection sensitivity of ~ 1.50 mJy for a velocity resolution of 6.4 km s $^{-1}$ within a redshift range of 0.11 – 0.66 for OHMs (Zhang et al. 2024), while the Arecibo Legacy Fast ALFA (ALFALFA) survey has a lower detection sensitivity of ~ 1.86 mJy beam $^{-1}$ after smoothing to a velocity resolution of 10 km s $^{-1}$ (Haynes et al. 2018). This suggests that the FASHI could detect more OHMs than ALFALFA. Furthermore, the Ultra-Wide Bandwidth (UWB) receiver on FAST can simultaneously cover a frequency range of 500–3300 MHz (or $z < 2.33$), making FAST a powerful instrument for observing OHMs in extragalactic objects (Zhang et al. 2023).

In this paper, we report 18 new and 9 old OHMs detected by FAST. Section 2 shows the FAST observations and source identification. Section 3 presents the characterization of the detected OHMs and lists four OHM-related catalogs. Section 4 discusses the hyperfine ratio, host galaxy properties, L_{OH} and L_{FIR} relationship, and FAST OHM detectability. Section 5 is a summary. Throughout this paper, we assume a Λ CDM cosmology with $H_0 = 75$ km s $^{-1}$ Mpc $^{-1}$, $\Omega_{\text{M}} = 0.3$, and $\Omega_{\Lambda} = 0.7$.

2. DATA AND IDENTIFICATION

2.1. Observational data

Observations were obtained from the FASHI project (Zhang et al. 2024), which uses the FAST 19-beam receiver to efficiently cover the FAST sky. The aperture of FAST is 500 m and the effective aperture is about 300 m, resulting in a beam size of $\sim 2.9'$ at 1.4 GHz. The full bandwidth of 500 MHz in the spectral line backend has a frequency coverage of 1000 to 1500 MHz with a total of 64k channels. The corresponding frequency resolution is 7.63 kHz or 1.6 km s $^{-1}$ at 1.4 GHz. The FASHI data are reduced using the FAST spectral data reduction pipeline HiFAST (Jing et al. 2024). The HiFAST pipeline combines data reduction packages including antenna temperature correction, baseline correction, RFI mitigation (Zhang et al. 2022), standing wave correction, gridding, flux correction (Liu et al. 2024), and data cube generation. The data have been smoothed to 6.4 km s $^{-1}$ spectral resolution per channel and the data cubes are gridded to

a pixel scale of $1'$. A heliocentric Doppler correction was applied to the data. A detailed observational setup and data reduction procedure is presented in the FASHI paper by Zhang et al. (2024).

2.2. Source identification

Extragalactic HI and OHM lines have similar spectral profiles at different redshifts. Spectroscopic redshift information is needed to distinguish them (Hess et al. 2021). The IRAS Point Source Catalog Redshift (PSCz) survey consists of spectroscopic redshifts, infrared and optical photometry, and miscellaneous information for 18351 IRAS sources, mostly selected from the Point Source Catalog (Saunders et al. 2000). The survey covers almost all galaxies with flux brighter than 0.595 Jy at 60 microns, over 84% of the sky. It is well known that most previously known OHMs have associated IRAS sources (e.g., Darling & Giovanelli 2000, 2001, 2002). To efficiently expand the OHM sample, we directly cross-checked the PSCz catalog (Saunders et al. 2000) with the corresponding FASHI data cube to see if there are any emission lines within a beam size of $2.9'$ and a velocity range of ~ 600 km s $^{-1}$. The FASHI data covers around 10000 deg 2 within $0^h \lesssim \text{RA} \lesssim 17^h$, $22^h \lesssim \text{RA} \lesssim 24^h$, $6^\circ \lesssim \text{Dec} \lesssim 0^\circ$, and $18^\circ \lesssim \text{Dec} \lesssim 64^\circ$ with a typical spectral detection sensitivity of ~ 1.50 mJy for a velocity resolution of ~ 6.4 km s $^{-1}$ at 1.4 GHz. Because the FASHI project can only operate in schedule-filler mode, parts of the above region are not fully covered. Within the region we found that there are a total of 145 PSCz sources covered by the current FASHI data with spectroscopic redshifts in the frequency range from 1304 to 1461 MHz. Using the FAST spectral data and the moment 0, 1, 2 images, we check the 145 sources one by one, including the redshift, coordinate, flux density, and the g , r , and z bands of the SDSS data, and then discard the probable HI sources as judged by the spectroscopic redshift information. In the end, we discovered and conformed 27 OHMs, 18 of which were first found by FAST. Detailed information on these sources is presented in the following sections.

3. DETECTION RESULTS AND ANALYSIS

3.1. OHM locations

In Figure 1 we show all the OHM locations, including 18 new OHMs found by FAST and 136 known ones found by others. From Figure 1 we can see that the previously known OHMs are mostly located at $0^\circ \lesssim \text{Dec} \lesssim 30^\circ$, covered by the Arecibo observations. It is expected that the FAST observation will be able to fill the gap of $\text{Dec} \gtrsim 30^\circ$ and $\text{Dec} \lesssim 0^\circ$. Currently, the area covered by FAST has reached ~ 10000 deg 2 . We have discov-

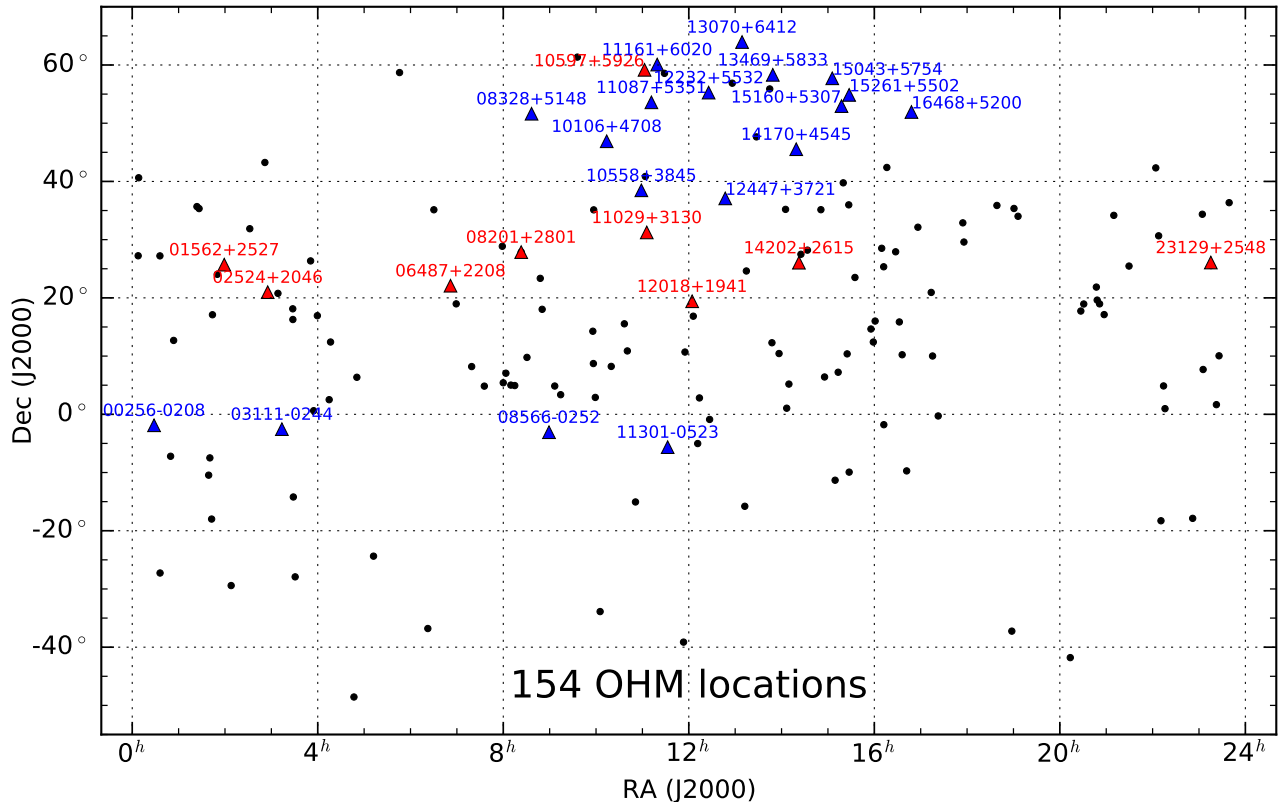


Figure 1. Locations for a total of 154 OHMs, including all previously known (Darling & Giovanelli 2002, 2006; Willett 2012; Suess et al. 2016; Hess et al. 2021; Glowacki et al. 2022; Jarvis et al. 2023) and 18 newly discovered OHMs in this work. The triangles with blue IRAS names are the 18 OHMs newly discovered by FAST, while the red ones are 9 known OHMs recovered by FAST. The black dots are OHMs previously discovered by others.

ered and identified 27 OHMs, which is 20% of all known OHMs, and including 18 newly found OHMs, which is 12.4% of all known OHMs. The 27 OHMs are selected and identified from the 145 PSCz sources, already covered by the current FAST observation. This means that the FAST OHM detection rate is 18.6%, which is close to the 17% detection rate of the Arecibo OHM survey (Darling & Giovanelli 2000). However, about 20 previously known OHMs with PSCz counterparts are not detected by FAST, although they lie within the volume surveyed by FASHI. The main reason for this is the currently limited detection sensitivity. Furthermore, it also means that about 47 (27+20) OHMs have been successfully detected in the 145 PSCz sources, resulting in a detection rate of 32.4% for this PSCz sample.

3.2. Individual sources

In Tables 1, 2, and 3 we list the parameters of 27 OHMs measured by FAST, including 18 newly discovered and 9 previously known sources. Of the latter, eight previously known sources were observed by the Arecibo OHM survey (Darling & Giovanelli 2000, 2001, 2002, 2006), and IRAS 10597+5926 was first found by Willett

(2012). For all nine previously known OHMs, the positions and redshifts of the optical counterparts (OCs) are in good agreement with those of the FAST OH observations. For all 27 OHMs, the OH spectra, integrated intensity distributions, and RGB images are shown in Figures 2 and 6, where both the radio and optical redshifts are given in the spectral panels, and the position of each OC is given in the OH integrated intensity map. In nearly all 27 OHMs, optical RGB images show typical merging systems with elongated tidal tails surrounding the nucleus. For IRAS 00256-0208, 10558+3845, 12018+1941, 12447+3721, 14170+4545, 14202+2615, 15043+5754, and 15160+5307, the detection sensitivities are low and they require more observation time for further confirmation. IRAS 08328+5148 is one of four OHMs for which the centroid of the FAST detection is relatively far away on the sky from the position of the putative optical counterpart. (The others, to differing degrees, are IRAS 03111-0244, IRAS 12447+3721, and IRAS 14202+2615.) These OHMs could be similar to IRAS 08328+5148, in that the true counterpart for the OHM might be a galaxy that is associated with, but not identical to, the “optical counterpart” with the match-

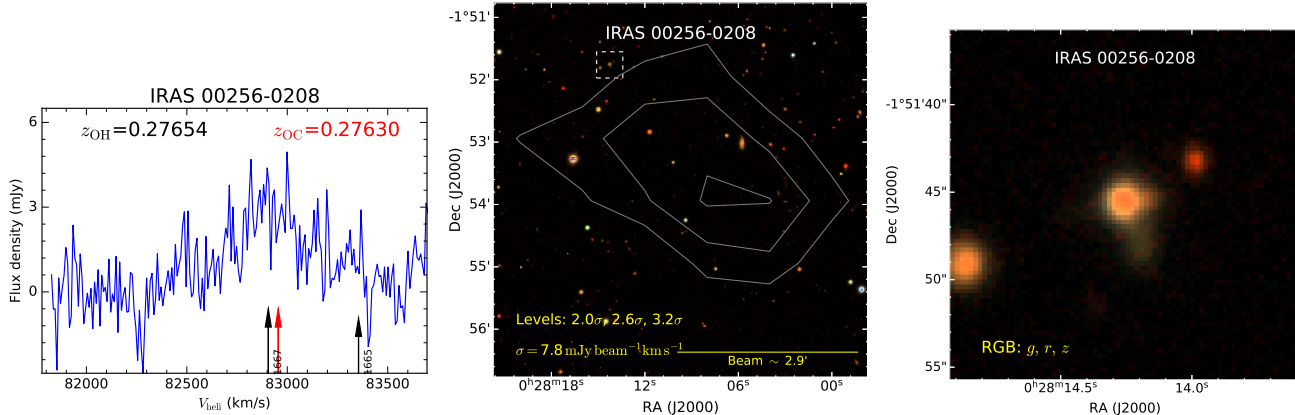


Figure 2. OHM IRAS 00256-0208. *Left:* FAST OH emission spectrum. The 1667 MHz OH redshift measured by FAST (in black) and an optical spectroscopic redshift (in red) are presented above and below the spectrum with text and corresponding colored arrows, respectively. The expected location of 1665 MHz OH line is indicated by a shorter arrow. *Middle:* Gray contours indicate the OH integrated intensity distribution seen by FAST with a beam size of $\sim 2.9'$. The contour levels are shown in the image. The background shows an RGB image of the g , r , and z bands of the SDSS data. The white square indicates the OC of the OHM. *Right:* The zoomed-in RGB image of the OC within the white square in the middle panel. The other 26 OHMs are shown in Figure 6.

ing spectroscopic redshift. Other notes for some of the OHMs are as follows:

IRAS 00256-0208 This OHM has the third highest redshift among all known OHMs in the main 1667 MHz OH emission lines, the highest being J095903.22+025356.1 with a redshift of $z_{\text{OH}} \sim 0.7092$, recently discovered by Jarvis et al. (2023).

IRAS 01562+2527¹ This has been confirmed as an OHM by the Arecibo OHM survey (Darling & Giovanelli 2002). This survey has a consistent detection result with FAST.

IRAS 02524+2046 This OHM was first confirmed by the Arecibo OHM survey (Darling & Giovanelli 2002), which detected an extremely strong peak reaching 40 mJy. However, the peak detected by FAST is 21.78 ± 1.83 mJy. This is probably because the OH flux density is time variable. The emission lines are strong and narrow and show an extremely good correspondence between the 1667 and 1665 MHz lines. This allows us to measure the hyperfine line ratio (see Table 2).

IRAS 06487+2208 This OHM was first found and reported by the Arecibo OHM survey (Darling & Giovanelli 2000). The optical spectrum of this source has been described as a composite of H II and LINER features based on the Osterbrock spectral line ratio classification method (Osterbrock 1989; Veilleux et al. 1995). The optical RGB image is unresolved, but there may be another nucleus or tidal tail to the north of the main nucleus.

¹ Listed as IRAS 01562+2528 by Darling & Giovanelli (2002)

IRAS 08201+2801 This has been confirmed as an OHM by the Arecibo OHM survey (Darling & Giovanelli 2001). Kim et al. (1998) classified the nucleus of this OHM as a starburst. The OH spectrum of this source shows multiple velocity components. In Figure 6, the optical RGB image shows an obvious interaction morphology with two nuclei connected by arcs and a single kinked tidal tail, clearly indicating an advanced merger (see also Darling & Giovanelli 2001).

IRAS 08328+5148 This is a newly discovered OHM (see Figure 6). To the east (OC-1 with RA, Dec = 129.1717° , 51.6246°) of the OC listed in Table 3, there is an optical spectroscopic object with a redshift of 0.237 from the SDSS catalog. However, the OC coordinates are $48''$ away from the OH emission center measured by FASHI. Fortunately, we find another optical object (named OC-2 with RA, Dec = 129.1505° , 51.6267°) at the center of the OH emission distribution. Although this object has no spectroscopic redshift, its SDSS photometric redshift is 0.234 ± 0.070 , which agrees well with the OH redshift of 0.23749. In addition, OC-1 and OC-2 have similar optical colors. Furthermore, the coordinates of IRAS 08328+5148 are in good agreement with the observed OH line coordinates. Therefore, it is likely that OC-2 is the optical counterpart of this OHM, but its spectroscopic redshift is needed for further confirmation.

IRAS 10106+4708 The source is bright in all four WISE bands, and the optical data display an evident tidal tail (see Figure 6). Despite that, the optical extinction is significant, leading to the absence of the $H\beta$ and [OIII] lines. WISE colors are estimated to be [4.6]-

[12] = 4.18 and [3.4]-[4.6] = 0.86, leading this object to be described as a dusty quasar (Nikutta et al. 2014).

IRAS 10597+5926 This OHM was first found and reported by Willett (2012), where the detected peak flux density is 17.56 mJy, while it is 32.27 ± 2.23 mJy measured by FAST. The flux densities are very different, but the line profiles are consistent between the two.

IRAS 11029+3130² This was first found and reported by the Arecibo OHM surveys (Darling & Giovanelli 2001). The central core is a LINER-type active galaxy nucleus (Alatalo et al. 2016).

IRAS 11087+5351 The 1665 MHz emission line is clearly visible. The measured line ratio is $R_{1667:1665} = 1.32 \pm 0.21$, which is the lowest measured ratio among all sources in this work. In Figure 6, the optical RGB image shows an extended morphology with a bright nucleus in the center. The central nucleus is optically identified as a LINER-type active galaxy nucleus by Toba et al. (2014).

IRAS 11161+6020 Toba et al. (2014) classified this object spectroscopically as a Seyfert 2 galaxy.

IRAS 11301-0523 In Figure 6 the optical RGB image shows an arc-like structure with several close and connected nuclei. The OH spectrum has multiple velocity components, and the 1665 MHz line is not visible.

IRAS 12447+3721 Duarte Puertas et al. (2017) classified it as a H II galaxy with a high star formation rate.

IRAS 13469+5833 The optical RGB image shows a possible merging system with several tidal tails surrounding the nuclei (see also the HST F814W-band images in Murata et al. 2017). The OH spectrum has double velocity components. The IRAS 13469+5833 is identified as an H II galaxy (Lin et al. 2018).

IRAS 14202+2615 This source has been observed by the Arecibo OHM surveys (Darling & Giovanelli 2000, 2006), but without sufficient sensitivity to see the OH emission line. In the FASHI survey we detected the OHM emission line with a peak flux density of 4.38 ± 1.15 mJy, at a SNR of only about 3 (see Figure 6). The optical redshift from Saunders et al. (2000) is in good agreement with the OH line measured by FAST, while the spatially projected coordinate offset is $\sim 2.0'$. The optical RGB image shows two close nuclei, one of which has a visible tidal tail. This morphology probably indicates a merging system.

IRAS 15160+5307 The OH spectrum has a weak peak of ~ 2.5 mJy, but the blue wing is broad and the red wing has an absorption feature.

IRAS 15261+5502 Hou et al. (2009) classified it as a starburst galaxy.

IRAS 16468+5200 Weedman & Houck (2008) classified it as a LINER-type active galaxy nucleus. In Figure 6 the optical RGB image shows a typical merging system with two interacting nuclei, one of which has an elongated tidal tail.

IRAS 23129+2548 This source has been confirmed as an OHM by the Arecibo OHM surveys (Darling & Giovanelli 2001). The nucleus of this OHM host is classified as a LINER by Veilleux et al. (1999).

3.3. OHM catalog

Table 1 presents the main properties of 27 OHMs detected by FASHI, including coordinates, redshift, line width, and flux. Each column in Table 1 is introduced as follows:

- Column 1: Index number for each FASHI extragalactic source. This index number is unique to each FASHI source.
- Column 2: Centroid coordinate (J2000) for the OH source in the format of `Jhhmmss.ss±ddmmss.s`.
- Column 3: IRAS source name (Helou & Walker 1988).
- Column 4-5: Right ascension (RA) and declination (Dec) in units of deg for the FASHI source centroid (J2000).
- Column 6: Redshift, z_{\odot} of the 1667 MHz OH line, corresponding to the heliocentric velocity in Column 7.
- Column 7: Heliocentric velocity of the OH source, cz_{\odot} in units of km s^{-1} . All results are presented in this work using the optical helio-centric definition of velocity.
- Column 8: Velocity width of the OH line profile, W_{50} in km s^{-1} , measured at the level of 50% of the peak.
- Column 9: OH line peak intensity, F_{peak} in mJy.
- Column 10: OH line noise level for the spatially integrated spectral profile, σ_{rms} in mJy. It was obtained by measuring over the signal and RFI free portions of the integrated HI spectrum at a spectral resolution of 6.4 km s^{-1} .

² listed as IRAS 11028+3130 by Darling & Giovanelli (2001)

Table 1. FASHI detected OHMs including coordinates, redshift, line width, peak flux.

[1]	[2]	[3]	[4]	[5]	[6]	[7]	[8]	[9]	[10]
FASHI ID	FASHI name J2000	IRAS name B1950	RA _{oh} deg	Dec _{oh} deg	z_{\odot}	V_{heli} km s ⁻¹	W_{50} km s ⁻¹	F_{peak} mJy	rms mJy
20240066172	J002814.52-015310.0	00256-0208	7.061	-1.886	0.27656	82912.1	279.6	3.05	0.88
20240066090	J015902.56+254224.7	01562+2527	29.761	25.707	0.16600	49766.2	272.8	6.72	1.43
20240066093	J025515.32+205835.5	02524+2046	43.814	20.977	0.18067	54164.0	86.4	21.78	1.83
20240066181	J031336.48-023255.8	03111-0244	48.402	-2.549	0.18956	56827.9	77.1	15.27	1.67
20240066097	J065143.27+220518.1	06487+2208	102.930	22.088	0.14347	43012.5	130.4	5.82	1.37
20240066055	J082310.95+275137.6	08201+2801	125.796	27.860	0.16793	50343.5	242.3	11.45	1.50
20240099047	J083634.98+513745.8	08328+5148	129.146	51.629	0.23749	71196.3	105.9	10.63	1.10
20240066185	J085909.64-030430.6	08566-0252	134.790	-3.075	0.20262	60743.1	190.2	7.73	1.27
20240066025	J101347.44+465356.6	10106+4708	153.448	46.899	0.20529	61543.0	159.4	24.73	1.32
20240066062	J105837.38+382836.6	10558+3845	164.656	38.477	0.20788	62319.4	26.3	4.35	1.04
20240066027	J110245.08+591005.0	10597+5926	165.688	59.168	0.19607	58780.0	236.2	32.27	2.23
20240066060	J110537.56+311427.4	11029+3130	166.407	31.241	0.19885	59613.8	130.2	3.36	0.97
20240066028	J111136.57+533514.0	11087+5351	167.902	53.587	0.14314	42913.0	101.9	3.65	0.87
20240129741	J111908.12+600432.5	11161+6020	169.784	60.076	0.26434	79246.5	288.2	9.07	2.05
20240066187	J113239.21-053833.9	11301-0523	173.163	-5.643	0.22984	68903.1	168.0	6.98	1.46
20240066105	J120420.53+192456.7	12018+1941	181.086	19.416	0.16783	50315.5	254.6	1.90	0.83
20240066030	J122539.49+551528.9	12232+5532	186.415	55.258	0.23250	69702.5	166.1	2.40	0.66
20240066069	J124709.66+370508.6	12447+3721	191.790	37.086	0.15847	47506.6	198.0	1.40	0.68
20240066013	J130854.87+635636.6	13070+6412	197.229	63.944	0.20523	61525.8	154.6	12.48	1.97
20240066035	J134841.23+581817.8	13469+5833	207.172	58.305	0.15716	47114.4	20.6	9.43	1.26
20240066034	J141859.45+453206.3	14170+4545	214.748	45.535	0.15009	44997.1	68.7	2.43	0.85
20240066110	J142227.98+260225.7	14202+2615	215.617	26.040	0.15925	47740.6	16.0	4.38	1.15
20240066037	J150535.42+574248.3	15043+5754	226.398	57.713	0.15029	45054.5	115.9	2.17	1.16
20240066039	J151732.61+525616.8	15160+5307	229.386	52.938	0.15227	45648.2	195.3	1.34	0.51
20240102609	J152725.70+545139.2	15261+5502	231.857	54.861	0.22902	68657.8	218.0	8.42	1.04
20240066042	J164800.26+515535.2	16468+5200	252.001	51.926	0.15032	45065.1	151.3	3.98	1.28
20240066122	J231519.36+260419.1	23129+2548	348.831	26.072	0.17881	53605.7	278.4	3.42	0.96

Notes. The IRAS names in bold are previously known OHMs, while the others are newly discovered by FAST.

3.4. Hyperfine ratio catalog

Table 2 presents the integrated flux and the hyperfine ratio between the 1667 and 1665 MHz lines. Each column in Table 2 is introduced as follows:

- Column 1: Index number for each FASHI extragalactic source. This index number is unique to each FASHI source.
- Column 2: IRAS source name.
- Column 3: Integrated flux of the 1667 MHz line, S_{int} , in mJy beam⁻¹km s⁻¹, summing all velocity channels containing signal within an appropriate velocity range from each integrated spectrum. The velocity range is listed in Columns 4 and 5.

- Columns 4-5: The minimum (V_{min}^{1667}) and maximum (V_{max}^{1667}) velocities of the integrated flux range for the 1667 MHz line.
- Column 6: Integrated flux of the 1665 MHz line, S_{int} , in mJy beam⁻¹km s⁻¹, summing all velocity channels containing signal within an appropriate velocity range from each integrated spectrum. The velocity range is listed in Columns 7 and 8.
- Columns 7-8: The minimum (V_{min}^{1665}) and maximum (V_{max}^{1665}) velocities of the integrated flux range for the 1665 MHz line.
- Column 9: Hyperfine line ratio between the 1667 and 1665 MHz lines.

3.5. OHM optical counterpart catalog

Table 2. Hyperfine ratio between the 1667 and 1665 MHz lines.

[1]	[2]	[3]	[4]	[5]	[6]	[7]	[8]	[9]
FASHI ID	IRAS name	S_{int}^{1667}	V_{min}^{1667}	V_{max}^{1667}	S_{int}^{1665}	V_{min}^{1665}	V_{max}^{1665}	$R_{1667:1665}$
		mJy·km s ⁻¹	km s ⁻¹	km s ⁻¹	mJy·km s ⁻¹	km s ⁻¹	km s ⁻¹	ratio
20240066172	00256-0208	1089.2 ± 65.1	82246.2	83457.0				
20240066090	01562+2527	2026.8 ± 93.5	49363.3	50148.7				
20240066093	02524+2046	1781.4 ± 59.1	54028.3	54243.2	607.3 ± 42.6	54065.6	54396.2	2.93 ± 0.23
20240066181	03111-0244	1167.6 ± 54.0	56703.8	56921.8	424.2 ± 57.8	56728.9	57181.4	2.75 ± 0.40
20240066097	06487+2208	848.0 ± 58.9	42839.9	43178.3	259.7 ± 46.8	42869.3	43121.6	3.27 ± 0.63
20240066055	08201+2801	2110.0 ± 77.8	50065.3	50568.3				
20240099047	08328+5148	1325.4 ± 50.6	70921.6	71376.2	140.4 ± 27.1	71142.6	71319.7	9.44 ± 1.85
20240066185	08566-0252	1427.1 ± 51.1	60584.7	60919.2				
20240066025	10106+4708	4011.7 ± 68.5	61332.6	61876.2				
20240066062	10558+3845	212.3 ± 46.7	62083.1	62492.4	130.7 ± 30.6	62179.0	62420.2	1.62 ± 0.52
20240066027	10597+5926	7259.4 ± 112.5	58535.6	59039.4	477.0 ± 45.2	58688.7	59067.3	15.22 ± 1.46
20240066060	11029+3130	424.8 ± 40.6	59463.6	59819.7				
20240066028	11087+5351	289.4 ± 27.2	42818.6	43005.8	219.1 ± 28.2	42797.8	43035.7	1.32 ± 0.21
20240129741	11161+6020	2468.3 ± 114.1	78901.6	79578.7				
20240066187	11301-0523	1014.8 ± 66.7	68669.5	69110.5				
20240066105	12018+1941	370.6 ± 37.4	50139.7	50530.3	80.8 ± 20.5	50276.9	50412.2	4.59 ± 1.25
20240066030	12232+5532	399.8 ± 26.0	69534.9	69869.2	259.2 ± 25.2	69535.6	69853.5	1.54 ± 0.18
20240066069	12447+3721	287.8 ± 33.0	47306.6	47749.7				
20240066013	13070+6412	2016.0 ± 91.6	61324.5	61764.1				
20240066035	13469+5833	556.0 ± 51.5	46975.8	47292.6				
20240066034	14170+4545	197.8 ± 36.1	44860.1	45194.9				
20240066110	14202+2615	319.4 ± 49.4	47601.5	47949.1				
20240066037	15043+5754	211.0 ± 44.5	44925.3	45202.0				
20240066039	15160+5307	305.5 ± 28.4	45368.5	45923.7				
20240102609	15261+5502	1857.3 ± 57.5	68312.8	68944.2				
20240066042	16468+5200	640.3 ± 57.8	44889.0	45267.6				
20240066122	23129+2548	845.4 ± 57.8	53272.0	53960.7				

Notes. The IRAS names in bold are previously known OHMs, while the others are newly discovered by FAST.

Table 3 presents the main properties of the OCs corresponding to the OHMs, including IRAS flux densities, and FIR properties. Each column in Table 3 is introduced as follows:

- Column 1: Index number for each FASHI extragalactic source. This index number is unique to each FASHI source.
- Column 2: IRAS source catalog name.
- Column 3-4: RA and Dec with centroid coordinate (J2000) in units of deg for OHM OCs extracted from the SDSS catalog.
- Column 5: Heliocentric optical redshift, z_{\odot} , extracted from the SDSS catalog.

- Column 6-7: IRAS 60 and 100 μm flux densities f_{60} and f_{100} in units of Jy (Helou & Walker 1988).
- Column 8: Luminosity distance D_L in h_{75}^{-1} Gpc, estimated with the cosmology calculator³ (Wright 2006).
- Column 9: Logarithm of the FIR luminosity L_{FIR} in units of $h_{75}^{-2} L_{\odot}$, estimated using the following equation from Sanders & Mirabel (1996) with

$$L_{\text{FIR}} = 3.96 \times 10^{11} D_L^2 (2.58 f_{60} + f_{100}), \quad (1)$$

where f_{60} and f_{100} are listed in Columns 6 and 7, and D_L in units of h_{75}^{-1} Gpc listed in Column 8.

³ <https://www.astro.ucla.edu/~wright/CosmoCalc.html>

Table 3. OHM optical counterparts including IRAS flux and FIR properties.

[1]	[2]	[3]	[4]	[5]	[6]	[7]	[8]	[9]	[10]
FASHI ID	IRAS name B1950	RA _{oc} deg	Dec _{oc} deg	z_{\odot} PSCz	f_{60} Jy	f_{100} Jy	D_L h_{75}^{-1} Gpc	$\log L_{\text{FIR}}$ $h_{75}^{-2} L_{\odot}$	$\log L_{\text{OH}}$ $h_{75}^{-2} L_{\odot}$
20240066172	00256-0208	7.059	-1.863	0.27630	0.65 ± 0.07	1.00 ± 0.00	1.320	12.27 ± 0.03	3.40 ± 0.03
20240066090	01562+2527	29.761	25.710	0.16580	0.80 ± 0.06	1.85 ± 0.15	0.744	11.93 ± 0.02	3.22 ± 0.02
20240066093	02524+2046	43.821	20.983	0.18153	0.94 ± 0.08	8.48 ± 0.00	0.817	12.46 ± 0.01	3.24 ± 0.01
20240066181	03111-0244	48.422	-2.560	0.18833	0.69 ± 0.06	1.03 ± 0.00	0.862	11.92 ± 0.02	3.09 ± 0.02
20240066097	06487+2208	102.941	22.074	0.14370	2.07 ± 0.17	2.36 ± 0.26	0.634	12.09 ± 0.03	2.71 ± 0.03
20240066055	08201+2801	125.803	27.861	0.16750	1.13 ± 0.09	1.60 ± 0.18	0.753	12.01 ± 0.03	3.24 ± 0.02
20240099047	08328+5148	129.150	51.627	0.23700	0.37 ± 0.11	1.58 ± 0.00	1.110	12.09 ± 0.05	3.35 ± 0.02
20240066185	08566-0252	134.789	-3.070	0.20201	0.79 ± 0.07	1.10 ± 0.00	0.928	12.03 ± 0.03	3.24 ± 0.02
20240066025	10106+4708	153.450	46.900	0.20481	0.77 ± 0.08	1.37 ± 0.30	0.942	12.07 ± 0.05	3.70 ± 0.01
20240066062	10558+3845	164.664	38.485	0.20660	0.70 ± 0.06	1.00 ± 0.00	0.955	12.01 ± 0.02	2.44 ± 0.10
20240066027	10597+5926	165.696	59.177	0.19583	1.02 ± 0.08	1.33 ± 0.17	0.895	12.10 ± 0.03	3.92 ± 0.01
20240066060	11029+3130	166.406	31.242	0.19890	1.04 ± 0.09	1.38 ± 0.11	0.909	12.12 ± 0.03	2.70 ± 0.04
20240066028	11087+5351	167.902	53.583	0.14270	1.00 ± 0.11	1.00 ± 0.13	0.632	11.75 ± 0.04	2.24 ± 0.04
20240129741	11161+6020	169.779	60.075	0.26428	0.61 ± 0.05	1.28 ± 0.19	1.253	12.25 ± 0.04	3.72 ± 0.02
20240066187	11301-0523	173.175	-5.663	0.23019	0.70 ± 0.07	1.42 ± 0.16	1.069	12.16 ± 0.03	3.21 ± 0.03
20240066105	12018+1941	181.102	19.419	0.16865	1.64 ± 0.18	1.86 ± 0.22	0.753	12.14 ± 0.04	2.49 ± 0.04
20240066030	12232+5532	186.410	55.264	0.23143	0.62 ± 0.06	1.63 ± 0.00	1.083	12.18 ± 0.02	2.81 ± 0.03
20240066069	12447+3721	191.782	37.094	0.15870	1.11 ± 0.12	1.00 ± 0.00	0.707	11.88 ± 0.04	2.33 ± 0.05
20240066013	13070+6412	197.231	63.941	0.20492	0.74 ± 0.05	0.71 ± 0.11	0.941	11.96 ± 0.03	3.40 ± 0.02
20240066035	13469+5833	207.167	58.315	0.15778	1.34 ± 0.11	1.99 ± 0.14	0.700	12.02 ± 0.02	2.60 ± 0.04
20240066034	14170+4545	214.745	45.537	0.15026	0.73 ± 0.06	1.19 ± 0.12	0.666	11.73 ± 0.03	2.11 ± 0.08
20240066110	14202+2615	215.631	26.035	0.15915	1.45 ± 0.16	1.95 ± 0.23	0.711	12.06 ± 0.04	2.38 ± 0.07
20240066037	15043+5754	226.415	57.719	0.15059	0.99 ± 0.07	1.42 ± 0.10	0.667	11.85 ± 0.02	2.14 ± 0.09
20240066039	15160+5307	229.374	52.947	0.15199	0.64 ± 0.03	1.38 ± 0.08	0.677	11.74 ± 0.02	2.32 ± 0.04
20240102609	15261+5502	231.861	54.864	0.22921	0.53 ± 0.05	1.00 ± 0.00	1.065	12.03 ± 0.03	3.47 ± 0.01
20240066042	16468+5200	252.006	51.929	0.15054	1.01 ± 0.07	1.61 ± 0.00	0.667	11.87 ± 0.02	2.63 ± 0.04
20240066122	23129+2548	348.839	26.076	0.17810	1.80 ± 0.20	1.70 ± 0.17	0.808	12.21 ± 0.04	2.90 ± 0.03

Notes. The IRAS names in bold are previously known OHMs, while the others are first discovered by FAST.

- Column 10: OH line luminosity L_{OH} in units of $h_{75}^{-2} L_{\odot}$. From the integrated line flux S_{int} we use the general relation for the spectral line luminosity (e.g., Briggs 1998) with

$$\frac{L_{\text{OH}}}{L_{\odot}} = \left(\frac{1.7064}{1 + z_{\text{OH}}} \right) \left(\frac{S_{\text{int}}}{\text{mJy km s}^{-1}} \right) \left(\frac{D_L}{\text{Gpc}} \right)^2, \quad (2)$$

where we take the stronger of the two main OH lines with a rest frequency of 1667.35903 MHz to define z_{OH} .

3.6. OHM catalog cross-matching with GSWLC

Table 4 shows the 28 sources recovered when all known 154 OHMs are cross-matched with the GALEX-SDSS-WISE Legacy Catalog (GSWLC) catalog (Salim et al. 2016) under the condition $\delta_{\text{RA}} \leq 3'$, $\delta_{\text{Dec}} \leq 3'$ and

$\delta_{\text{HI velocity}} \leq 300 \text{ km s}^{-1}$. Nine of these 28 OHMs are detected by FAST. Each column in Table 3 is introduced as follows:

- Column 1: IRAS source catalog name.
- Column 2: OBJID, SDSS photometric identification number, from GSWLC.
- Column 3-4: RA and Dec with centroid coordinate (J2000) in units deg, from GSWLC.
- Column 5: Redshift, z_{\odot} , from GSWLC.
- Column 6: Stellar mass, $\log(M_{\star})$ with its error, from GSWLC.
- Column 7: UV/optical (SED) star formation rate, $\log(\text{SFR}_{\text{SED}})$ with its error, from GSWLC.

Table 4. Cross-matched sources between all the known 154 OHMs and GSWLC.

[1]	[2]	[3]	[4]	[5]	[6]	[7]	[8]
IRAS name	OBJID	RA	Dec	z_{\odot}	$\log(M_{\star})$	$\log(\text{SFR}_{\text{SED}})$	A_V
B1950		deg	deg		M_{\odot}	$M_{\odot} \text{ yr}^{-1}$	mag
07556+2859	1237657629506142647	119.727	28.886	0.1262	10.70 ± 0.03	-0.54 ± 0.71	0.24 ± 0.10
08122+0505	1237660668730408974	123.723	4.937	0.1033	11.04 ± 0.04	0.57 ± 0.24	0.43 ± 0.16
08449+2332	1237664834854518934	131.959	23.353	0.1517	10.71 ± 0.06	1.47 ± 0.05	0.47 ± 0.06
09039+0503	1237658423543595297	136.642	4.858	0.1250	10.81 ± 0.03	1.56 ± 0.06	0.86 ± 0.06
09116+0334	1237654605316358298	138.574	3.365	0.1460	10.91 ± 0.03	0.43 ± 0.16	0.23 ± 0.10
09320+6134	1237651272966275163	143.965	61.353	0.0394	11.25 ± 0.03	1.16 ± 0.01	0.75 ± 0.00
09531+1430	1237671261205495893	148.958	14.269	0.2152	11.34 ± 0.04	1.00 ± 0.18	0.62 ± 0.12
09540+3521	1237664669506863314	149.246	35.119	0.1006	10.72 ± 0.03	0.36 ± 0.23	0.59 ± 0.11
10378+1108	1237661949170155593	160.122	10.888	0.1363	11.03 ± 0.03	1.57 ± 0.02	0.82 ± 0.03
10558+3845	1237664668975562850	164.664	38.485	0.2081	11.01 ± 0.09	1.56 ± 0.14	0.69 ± 0.14
11011+4107	1237662194520293391	165.976	40.850	0.0348	9.97 ± 0.14	0.58 ± 0.18	0.49 ± 0.11
11087+5351	1237657590319022140	167.902	53.583	0.1429	10.91 ± 0.07	1.44 ± 0.20	0.73 ± 0.18
11257+5850	1237655107301277787	172.140	58.563	0.0105	10.40 ± 0.04	0.85 ± 0.08	0.86 ± 0.09
12018+1941	1237667914881892435	181.102	19.419	0.1679	10.89 ± 0.09	1.44 ± 0.12	0.60 ± 0.15
12447+3721	1237664672714653739	191.782	37.094	0.1582	10.39 ± 0.09	0.96 ± 0.18	0.24 ± 0.15
13254+4754	1237661149769760972	201.900	47.647	0.0607	9.77 ± 0.07	0.33 ± 0.08	0.17 ± 0.08
13428+5608	1237661387602853939	206.176	55.887	0.0373	10.77 ± 0.05	0.35 ± 0.33	0.39 ± 0.14
13469+5833	1237659326015537309	207.167	58.314	0.1575	11.00 ± 0.05	0.90 ± 0.14	0.40 ± 0.14
14202+2615	1237665441523957822	215.631	26.035	0.1587	11.05 ± 0.05	1.38 ± 0.02	0.20 ± 0.02
14312+2825	1237665351854784676	218.365	28.200	0.1748	11.30 ± 0.09	1.59 ± 0.05	0.73 ± 0.08
14488+3521	1237662305655717891	222.726	35.144	0.2057	11.41 ± 0.04	2.23 ± 0.02	0.73 ± 0.01
15043+5754	1237671769072206053	226.415	57.719	0.1506	10.67 ± 0.06	1.29 ± 0.10	0.44 ± 0.14
15160+5307	1237655463779631232	229.374	52.946	0.1522	11.21 ± 0.06	1.47 ± 0.08	0.37 ± 0.11
15224+1033	1237662636908478686	231.213	10.380	0.1346	10.78 ± 0.05	1.13 ± 0.05	0.34 ± 0.03
15250+3608	1237662335714852881	231.748	35.977	0.0552	10.63 ± 0.04	0.97 ± 0.06	0.38 ± 0.06
15327+2340	1237665537075511390	233.738	23.504	0.0184	10.87 ± 0.02	0.37 ± 0.08	0.69 ± 0.07
16145+4231	1237665356696846411	244.050	42.400	0.0232	9.76 ± 0.04	-0.33 ± 0.10	0.19 ± 0.09
16300+1558	1237665536008520057	248.089	15.863	0.2418	11.20 ± 0.09	1.71 ± 0.13	0.49 ± 0.15

Notes. The listed Columns [2]-[8] in this catalog are extracted from GSWLC (Salim et al. 2016).

- Column 8: Dust attenuation, A_V , in rest-frame V , from GSWLC.

4. DISCUSSION

4.1. Hyperfine ratio

The 1667 and 1665 MHz lines refer to the main lines of OH at the radio rest frequencies of 1667.359 and 1665.402 MHz, while two satellite lines are located at 1720.530 and 1612.231 MHz (Radford 1964). In local thermodynamic equilibrium (LTE), the OH line ratios are approximately 1:5:9:1 for 1612, 1665, 1667, and 1720 MHz lines (Henkel et al. 1991; Hess et al. 2021). The 1667 MHz line is relatively common in extragalactic observations, but the 1665 MHz line is very rare because of its weakness. McBride et al. (2013) reported

that the hyperfine line ratio is $1 < R_{1667:1665} < 10$ with an average of $R_{1667:1665} \approx 5$. In previous observations (e.g., Darling & Giovanelli 2000, 2001, 2002), the 1667 and 1665 MHz lines often blend into each other, resulting in a barely measurable line ratio. The main reason for this is the inherently large line width ($> 500 \text{ km s}^{-1}$) of the 1667 MHz line. In Table 2 we present the hyperfine line ratio between the integrated fluxes of 1667 and 1665 MHz. In total we have detected 27 OHMs, 9 of which show a visible 1665 MHz line. The detection rate is 33.3% for the 1665 MHz line. For detected sources, the line ratio $R_{1667:1665}$ ranges from 1.32 to 15.22, with an average of $R_{1667:1665} = 4.74$, in agreement with the results reported by McBride et al. (2013). Although the hyperfine ratio is often consis-

tent with the thermal emission condition (Baan et al. 1982), e.g. for IRAS10558+3845 with $R_{1667:1665} = 1.62 \pm 0.52$, 11087+5351 with $R_{1667:1665} = 1.32 \pm 0.21$, and 12232+5532 with $R_{1667:1665} = 1.54 \pm 0.18$, which have relatively low hyperfine ratios with $R_{1667:1665} < 2$, McBride et al. (2013) suggested that the OH emission probably includes a significant non-thermal contribution. Furthermore, the wide range from 1.32 to 15.22 is indicative of complex maser pumping mechanisms.

4.2. Host galaxy properties

As expected, since the OHM sample was selected by cross-correlation with the IRAS-selected PSCz, which contains only objects with $60\mu\text{m}$ flux densities $> 0.595\text{ Jy}$, all of our detected OHMs are hosted by Luminous Infrared Galaxies (LIRGs) with $L_{\text{FIR}} > 10^{11}L_{\odot}$, or ultra-luminous infrared galaxies (ULIRGs) with FIR luminosities $L_{\text{FIR}} > 10^{12}L_{\odot}$ (e.g., Darling & Giovanelli 2002). 13 OHMs are ULIRGs and 14 OHMs are LIRGs based on the measured L_{FIR} , which ranges from $10^{11.70 \pm 0.03}$ to $10^{12.43 \pm 0.01}L_{\odot}$ with a median of $10^{12.00 \pm 0.02}L_{\odot}$. This means that all of the 27 OHMs have relatively high FIR luminosities. The strong FIR emission suggest that such 27 OHMs has undergone a very recent and strong starburst (e.g., Sanders & Mirabel 1996).

The majority of [U]LIRGs or OHMs show evidence of interaction with other galaxies or have recently undergone a galaxy merger (Andreasian & Alloin 1994; Darling & Giovanelli 2002). Mergers could be a way to funnel molecular gas into the core of the [U]LIRG, producing high molecular densities and stimulating the high star formation rates (Burdiuzha & Vikulov 1990). Pihlström (2007) suggested that the maser emission may originate in thick, circumnuclear structures, based on the results of high-resolution imaging.

OHMs are likely a disturbed system in a galaxy merger, as evidenced by tidal tails (Clements et al. 1996). We found that almost all of the 27 OHMs have recently merged or interacted with another galaxy (see Figures 2 and 6). This could be an indication that such galaxy system is in the process of merging as seen in the optical morphology (see Figures 2 and 6). In general, OHM line emission is always detected in [U]LIRGs (e.g., Darling 2007; Henkel & Wilson 1990; Suess et al. 2016; Willett 2012). It is likely that OHMs occur during a particular state or stage of the merger, which are consequences of tidal density enhancements that accompany galaxy interactions (Darling 2007). In fact, very-long-baseline interferometry (VLBI) radio images of Arp220 show that the OHM emission arises in regions only a few parsecs in size in its core, and have been used to

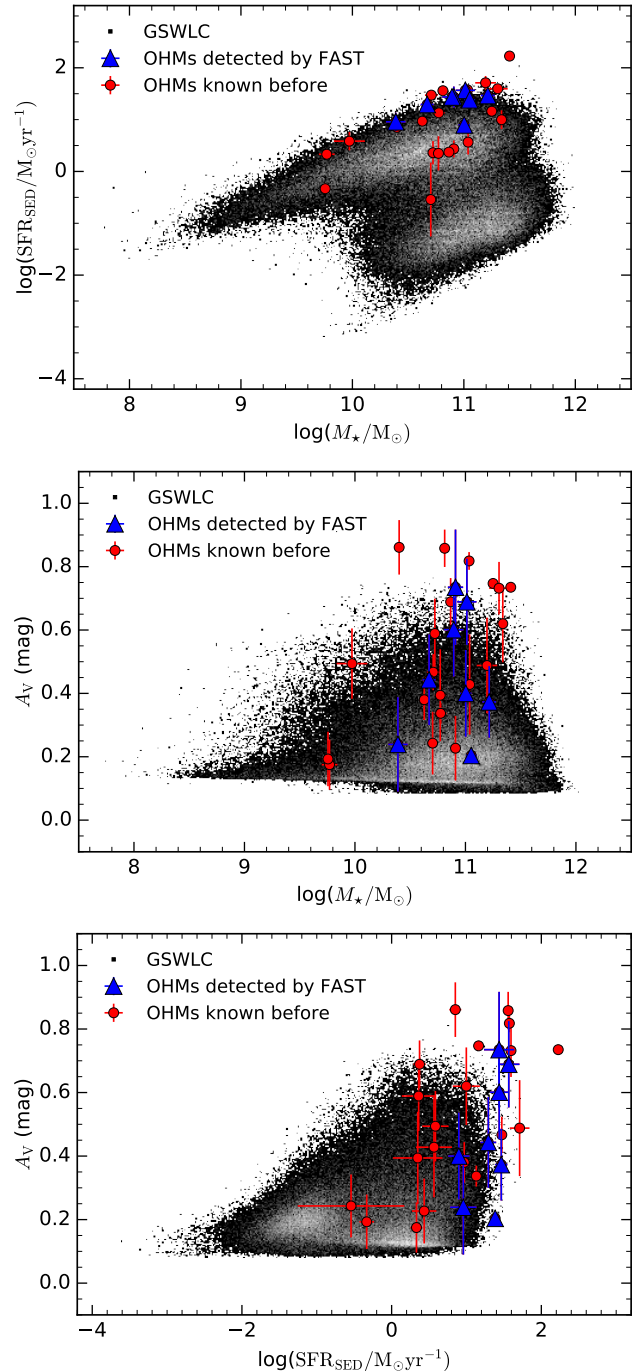


Figure 3. Two-dimensional distributions of $\log(M_*)$, $\log(\text{SFR}_{\text{SED}})$, and A_v . The background shows all the data in the GSWLC. The blue triangles indicate cross-matched OHMs detected by FAST. The red dots indicate an additional 19 cross-matched OHMs not detected by FAST among the 154 known OHMs.

support active galactic nucleus (AGN) models for this galaxy (Skinner et al. 1997).

The multi-wavelength SED fitting results in Figure 3 also show that the OH host galaxies are massive ($M_* \simeq 10^{11} M_\odot$) galaxies with the SFR above the star-forming main sequence. The higher A_V value of the OH galaxies from the SED fit is also consistent with the high IR luminosities. On the other hand, not all ULIRGs have detectable OH emission, suggesting that the OH emission may be triggered within a specific stage of the merger or may be seen by orientation effects. High-resolution OH mapping observations, e.g. with the Very Large Array (VLA), are still needed to better constrain the physical origin of the OH emission.

4.3. L_{OH} and L_{FIR} Relationship

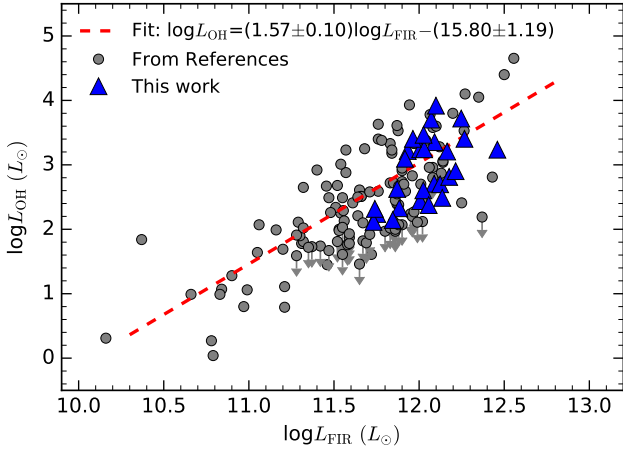


Figure 4. L_{OH} vs. L_{FIR} distribution including 154 sources. The blue triangles indicate OHMs discovered by FASHI. The grey dots indicate previously known OHMs (Darling & Giovanelli 2002, 2006; Willett 2012; Suess et al. 2016; Hess et al. 2021; Glowacki et al. 2022; Jarvis et al. 2023), where the sources with L_{OH} having only an upper limit are excluded from the current fitting statistics. The red dashed line shows the fitting result of the $L_{\text{OH}}-L_{\text{FIR}}$ relation.

OHMs are thought to be radiatively pumped by the FIR radiation field at 35 and 53 μm , with masing stimulated by 18 cm continuum emission from the surrounding environment (Henkel et al. 1987). In a simple scenario of low-gain unsaturated masing, the maser power is proportional to the pumping rate and the stimulated emission rate (Baan 1989). If the observed OHM represents an ensemble of many individual masing regions with different saturation states, then the relationship between OH and FIR luminosity is $L_{\text{OH}} \propto L_{\text{FIR}}^{1 < \gamma < 2}$ (Baan 1989; Darling & Giovanelli 2002; Yun et al. 2001). The measurement of γ has been frustrated by

small samples, survey bias, and theoretical bias. Darling & Giovanelli (2002) derived the relationship between OH and far IR luminosity with 95 data points as $\log L_{\text{OH}} = (1.57 \pm 0.11) \log L_{\text{FIR}} - (15.76 \pm 1.22)$. In this work we detect 27 OHMs and 18 new OHMs, plus 127 other previously known OHMs with OH and FIR luminosities from the literature (Darling & Giovanelli 2002, 2006; Willett 2012; Suess et al. 2016; Hess et al. 2021; Glowacki et al. 2022), where 31 sources with L_{OH} having only an upper limit are excluded from the current fitting statistics. Using the least-squares fitting method, the samples produce a fitting result with $\log L_{\text{OH}} = (1.57 \pm 0.10) \log L_{\text{FIR}} - (15.80 \pm 1.19)$ in Figure 4. The $\gamma = 1.57 \pm 0.10$ agrees well with the result of Darling & Giovanelli (2002) with $\gamma = 1.57 \pm 0.11$. Therefore, γ remains almost the same when the OHM samples reach up to 154, which is ~ 1.6 times the number of previously known OHMs.

4.4. FAST OHM detectability

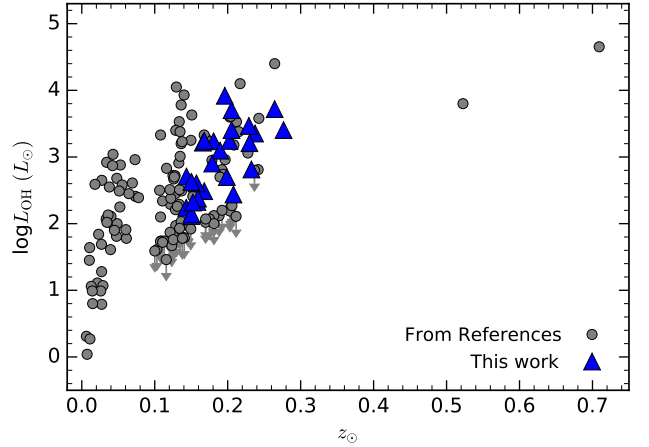


Figure 5. L_{OH} vs. z_\odot distribution including 154 sources. The blue triangles indicate 18 new found OHMs by FASHI. The grey dots indicate detections of previously known OHMs (Darling & Giovanelli 2002, 2006; Willett 2012; Suess et al. 2016; Hess et al. 2021; Glowacki et al. 2022; Jarvis et al. 2023). Each grey dot with a down arrow indicates the source with L_{OH} having only an upper limit.

Currently, the highest redshift detection of such an OHM in the main 1667 MHz OH emission line is J095903.22+025356.1 with a redshift of $z_{\text{OH}} = 0.7092$, recently found by Jarvis et al. (2023). The second highest is LADUMA J033046.20-275518.1 with a redshift of $z_{\text{OH}} = 0.5225$, found by Glowacki et al. (2022). However, the third highest redshift of OHMs is IRAS 00256-0208 with $z_{\text{OH}} = 0.27656$, found in this paper. The large gap (see Figure 5) between the three highest redshifts of OHMs requires more observatories to complete

the OHM picture. The 19-beam receiver with FAST is capable of simultaneously covering a frequency range of 1000-1500 MHz, and the Ultra-Wide Bandwidth (UWB) receiver with FAST could simultaneously cover 500-3300 MHz. FAST will be a powerful instrument for observing highly redshifted OH emission in extragalactic objects (Zhang et al. 2023).

Furthermore, radio frequency interference (RFI) always affects the search results of astronomical observations for all radio telescopes on Earth. At present, the redshifts of all known OHMs are mainly below $z \approx 0.27$ or $f \approx 1310$ MHz (Darling & Giovanelli 2002; Willett 2012; Haynes et al. 2018; Suess et al. 2016; Hess et al. 2021; Roberts et al. 2021), which is mainly due to the existence of strong RFI above $z \approx 0.27$. From the statistics of RFI in the FAST 19-beam array (Zhang et al. 2023), we can see that there is a lot of seriously strong RFI from communication and navigation satellites, over two broad frequency bands in 1150-1310 and 1465-1500 MHz, corresponding to a redshift of $0.27 \lesssim z \lesssim 0.45$ and $0.11 \lesssim z \lesssim 0.14$, respectively. It is because the frequency band in 1310-1465 MHz is very clear that FAST has already detected 27 OHMs in this band. In addition, the RFI is bearable in the frequency band of 1050-1150 MHz or $0.45 \lesssim z \lesssim 0.55$. Therefore, it is feasible to search for potential OHMs within $0.45 \lesssim z \lesssim 0.55$ using FASHI data in the future.

Moreover, the FASHI data have detected 27 OHMs in the frequency range 1310-1465 MHz with a typical spectral detection sensitivity of ~ 1.50 mJy at a spectral resolution of ~ 6.4 km s⁻¹ at 1.4 GHz (Zhang et al. 2024). The coverage of the current FASHI data is ~ 10000 deg². If FASHI observations cover ~ 20000 deg² in the future, FASHI is expected to obtain a total of 54 OHMs at the current detection sensitivity. If a longer integration time than the current FASHI drift survey is applied to each PSCz source, more OHMs would be extracted. Please note that the method of source identification in this work is to directly compare the PSCz catalog with the corresponding FASHI data cube to see if there are any emission lines (see Section 2.2). A blind and complete OHM identification throughout the FASHI data cube would expand the sample again, especially if OHMs can be hosted by galaxies with sub-LIRG far-IR luminosities. Thus, FASHI or FAST could provide great opportunities to detect more samples.

5. SUMMARY

The FAST All Sky HI survey (FASHI) aims to cover the entire sky observable by the Five-hundred-meter Aperture Spherical radio Telescope (FAST), covering ~ 22000 square degrees of declination between -14° and

$+66^\circ$, and in the frequency range of 1000-1500 MHz, with an expectation of detecting more than 100000 HI sources finally. At present, FASHI has observed more than 7600 square degrees. It has a typical spectral detection sensitivity of ~ 1.50 mJy for a velocity resolution of ~ 6.4 km s⁻¹ at a frequency of ~ 1.4 GHz. As of now, a total of 41741 extragalactic HI sources have been detected and released by FASHI.

To efficiently expand the OHM sample, we have directly cross-checked the PSCz catalog with the corresponding FASHI data cube. From 145 PSCz sources already covered by FASHI, we obtained 27 OHMs with a detection rate of 18.6%, including 9 previously known and 18 new ones, within a redshift range of $0.14314 \lesssim z_{\text{OH}} \lesssim 0.27656$. For 9 of the detected 27 OHMs, we also measured the hyperfine line ratio between the integrated fluxes of 1667 and 1665 MHz. The detection rate is 33.3% for the 1665 MHz line. The line ratio $R_{1667:1665}$ ranges from 1.32 to 15.22, with an average of $R_{1667:1665} = 4.74$, in agreement with the results reported by McBride et al. (2013).

We now have a total of 154 OHMs, including the 18 OHMs newly detected by FASHI. The full sample yields an L_{OH} and L_{FIR} relationship with $\log L_{\text{OH}} = (1.57 \pm 0.10)\log L_{\text{FIR}} - (15.80 \pm 1.19)$, which agrees well with the result of Darling & Giovanelli (2002) that $\gamma = 1.57 \pm 0.11$ from 95 data points. This indicates that γ remains almost the same when the OHM samples reach up to ~ 1.6 times the previously known OHMs.

Of the detected 27 OHMs of this work, 13 OHMs are ULIRGs and 14 OHMs are LIRGs, ranging from $10^{11.70 \pm 0.03}$ to $10^{12.43 \pm 0.01} L_{\odot}$ with a median of $10^{12.00 \pm 0.02} L_{\odot}$. As expected, all 27 OHMs have relatively high FIR luminosities. This is because the OHM sample was selected by cross-correlation with the IRAS-selected PSCz. The multi-wavelength SED fitting results also show that the OH host galaxies for such 27 OHMs are massive ($M_{\star} \simeq 10^{11} M_{\odot}$) galaxies with SFRs that place them above the star-forming main sequence. The higher A_V values for the OH hosts from the SED fit are also consistent with the high IR luminosities. On the other hand, not all ULIRGs have detectable OH emission, suggesting that the OH emission may be triggered within a specific stage of the merger or may have its visibility limited by orientation effects.

FAST, with its 19-beam array and UWB receiver, will be a powerful tool for observing more OHMs and unraveling their mystery in the future.

ACKNOWLEDGEMENTS

This work is supported by the National Key R&D Program of China (2022YFA1602901). CPZ acknowledges

support by the West Light Foundation of the Chinese Academy of Sciences (CAS). CC and JLX are supported by the National Natural Science Foundation of China, Nos. 11803044, 11933003, 12173045, and 11933011. This work is sponsored (in part) by the Chinese Academy of Sciences (CAS), through a grant to the CAS South America Center for Astronomy (CASSACA). We acknowledge the science research grants from the China Manned Space Project with No. CMS-CSST-2021-A05. We also wish to thank the anonymous referee for comments that improved the clarity of the paper.

FAST is a Chinese national mega-science facility, operated by the National Astronomical Observatories of Chinese Academy of Sciences (NAOC). SDSS acknowledges support and resources from the Center for High-Performance Computing at the University of Utah. The SDSS web site is www.sdss4.org. SDSS is managed by the Astrophysical Research Consortium for the Participating Institutions of the SDSS Collaboration including the Brazilian Participation Group, the Carnegie Institution for Science, Carnegie Mellon University, Center

for Astrophysics — Harvard & Smithsonian (CfA), the Chilean Participation Group, the French Participation Group, Instituto de Astrofísica de Canarias, The Johns Hopkins University, Kavli Institute for the Physics and Mathematics of the Universe (IPMU) / University of Tokyo, the Korean Participation Group, Lawrence Berkeley National Laboratory, Leibniz Institut für Astrophysik Potsdam (AIP), Max-Planck-Institut für Astronomie (MPIA Heidelberg), Max-Planck-Institut für Astrophysik (MPA Garching), Max-Planck-Institut für Extraterrestrische Physik (MPE), National Astronomical Observatories of China, New Mexico State University, New York University, University of Notre Dame, Observatório Nacional / MCTI, The Ohio State University, Pennsylvania State University, Shanghai Astronomical Observatory, United Kingdom Participation Group, Universidad Nacional Autónoma de México, University of Arizona, University of Colorado Boulder, University of Oxford, University of Portsmouth, University of Utah, University of Virginia, University of Washington, University of Wisconsin, Vanderbilt University, and Yale University.

REFERENCES

- Alatalo, K., Cales, S. L., Rich, J. A., et al. 2016, *ApJS*, 224, 38, doi: [10.3847/0067-0049/224/2/38](https://doi.org/10.3847/0067-0049/224/2/38)
- Andreasian, N., & Alloin, D. 1994, *A&AS*, 107, 23
- Baan, W. A. 1989, *ApJ*, 338, 804, doi: [10.1086/167237](https://doi.org/10.1086/167237)
- Baan, W. A. 1991, in *Astronomical Society of the Pacific Conference Series*, Vol. 16, *Atoms, Ions and Molecules: New Results in Spectral Line Astrophysics*, ed. A. D. Haschick & P. T. P. Ho, 45
- Baan, W. A., Rhoads, J., Fisher, K., Altschuler, D. R., & Haschick, A. 1992, *ApJL*, 396, L99, doi: [10.1086/186526](https://doi.org/10.1086/186526)
- Baan, W. A., Wood, P. A. D., & Haschick, A. D. 1982, *ApJL*, 260, L49, doi: [10.1086/183868](https://doi.org/10.1086/183868)
- Briggs, F. H. 1998, *A&A*, 336, 815, doi: [10.48550/arXiv.astro-ph/9710143](https://doi.org/10.48550/arXiv.astro-ph/9710143)
- Burdiuzha, V. V., & Vikulov, K. A. 1990, *MNRAS*, 244, 86
- Clements, D. L., Sutherland, W. J., McMahon, R. G., & Saunders, W. 1996, *MNRAS*, 279, 477, doi: [10.1093/mnras/279.2.477](https://doi.org/10.1093/mnras/279.2.477)
- Darling, J. 2007, *ApJL*, 669, L9, doi: [10.1086/523756](https://doi.org/10.1086/523756)
- Darling, J., & Giovanelli, R. 2000, *AJ*, 119, 3003, doi: [10.1086/301403](https://doi.org/10.1086/301403)
- . 2001, *AJ*, 121, 1278, doi: [10.1086/319413](https://doi.org/10.1086/319413)
- . 2002, *AJ*, 124, 100, doi: [10.1086/341166](https://doi.org/10.1086/341166)
- . 2006, *AJ*, 132, 2596, doi: [10.1086/508513](https://doi.org/10.1086/508513)
- Duarte Puertas, S., Vilchez, J. M., Iglesias-Páramo, J., et al. 2017, *A&A*, 599, A71, doi: [10.1051/0004-6361/201629044](https://doi.org/10.1051/0004-6361/201629044)
- Giovanelli, R., & Haynes, M. P. 2015, *A&A Rv*, 24, 1, doi: [10.1007/s00159-015-0085-3](https://doi.org/10.1007/s00159-015-0085-3)
- Glowacki, M., Collier, J. D., Kazemi-Moridani, A., et al. 2022, *ApJL*, 931, L7, doi: [10.3847/2041-8213/ac63b0](https://doi.org/10.3847/2041-8213/ac63b0)
- Haynes, M. P., Giovanelli, R., Kent, B. R., et al. 2018, *ApJ*, 861, 49, doi: [10.3847/1538-4357/aac956](https://doi.org/10.3847/1538-4357/aac956)
- Helou, G., & Walker, D. W. 1988, 0, <https://www.osti.gov/biblio/6458812>
- Henkel, C., Baan, W. A., & Mauersberger, R. 1991, *A&A Rv*, 3, 47, doi: [10.1007/BF00873457](https://doi.org/10.1007/BF00873457)
- Henkel, C., Guesten, R., & Baan, W. A. 1987, *A&A*, 185, 14
- Henkel, C., & Wilson, T. L. 1990, *A&A*, 229, 431
- Hess, K. M., Roberts, H., Dénes, H., et al. 2021, *A&A*, 647, A193, doi: [10.1051/0004-6361/202040019](https://doi.org/10.1051/0004-6361/202040019)
- Hou, L. G., Wu, X.-B., & Han, J. L. 2009, *ApJ*, 704, 789, doi: [10.1088/0004-637X/704/1/789](https://doi.org/10.1088/0004-637X/704/1/789)
- Jarvis, M. J., Heywood, I., Jewell, S. M., et al. 2023, *arXiv e-prints*, arXiv:2312.04345, <https://arxiv.org/abs/2312.04345>
- Jiang, P., Yue, Y., Gan, H., et al. 2019, *Science China Physics, Mechanics, and Astronomy*, 62, 959502, doi: [10.1007/s11433-018-9376-1](https://doi.org/10.1007/s11433-018-9376-1)

- Jiang, P., Tang, N.-Y., Hou, L.-G., et al. 2020, *Research in Astronomy and Astrophysics*, 20, 064, doi: [10.1088/1674-4527/20/5/64](https://doi.org/10.1088/1674-4527/20/5/64)
- Jing, Y., Wang, J., Xu, C., et al. 2024, *Science China Physics, Mechanics, and Astronomy*, 67, 259514, doi: [10.1007/s11433-023-2333-8](https://doi.org/10.1007/s11433-023-2333-8)
- Kim, D. C., Veilleux, S., & Sanders, D. B. 1998, *ApJ*, 508, 627, doi: [10.1086/306409](https://doi.org/10.1086/306409)
- Lin, Y.-T., Huang, H.-J., & Chen, Y.-C. 2018, *AJ*, 155, 188, doi: [10.3847/1538-3881/aab5b4](https://doi.org/10.3847/1538-3881/aab5b4)
- Liu, Z., Wang, J., Jing, Y., et al. 2024, arXiv e-prints, arXiv:2406.08278, doi: [10.48550/arXiv.2406.08278](https://doi.org/10.48550/arXiv.2406.08278)
- Lo, K. Y. 2005, *ARA&A*, 43, 625, doi: [10.1146/annurev.astro.41.011802.094927](https://doi.org/10.1146/annurev.astro.41.011802.094927)
- Lockett, P., & Elitzur, M. 2008, *ApJ*, 677, 985, doi: [10.1086/533429](https://doi.org/10.1086/533429)
- McBride, J., Heiles, C., & Elitzur, M. 2013, *ApJ*, 774, 35, doi: [10.1088/0004-637X/774/1/35](https://doi.org/10.1088/0004-637X/774/1/35)
- Murata, K. L., Yamada, R., Oyabu, S., et al. 2017, *MNRAS*, 472, 39, doi: [10.1093/mnras/stx1902](https://doi.org/10.1093/mnras/stx1902)
- Nan, R., Li, D., Jin, C., et al. 2011, *International Journal of Modern Physics D*, 20, 989, doi: [10.1142/S0218271811019335](https://doi.org/10.1142/S0218271811019335)
- Nikutta, R., Hunt-Walker, N., Nenkova, M., Ivezić, Ž., & Elitzur, M. 2014, *MNRAS*, 442, 3361, doi: [10.1093/mnras/stu1087](https://doi.org/10.1093/mnras/stu1087)
- Osterbrock, D. E. 1989, *Astrophysics of gaseous nebulae and active galactic nuclei*
- Pihlström, Y. M. 2007, in *Astrophysical Masers and their Environments*, ed. J. M. Chapman & W. A. Baan, Vol. 242, 446–451, doi: [10.1017/S1743921307013579](https://doi.org/10.1017/S1743921307013579)
- Radford, H. E. 1964, *PhRvL*, 13, 534, doi: [10.1103/PhysRevLett.13.534](https://doi.org/10.1103/PhysRevLett.13.534)
- Roberts, H., Darling, J., & Baker, A. J. 2021, *ApJ*, 911, 38, doi: [10.3847/1538-4357/abe944](https://doi.org/10.3847/1538-4357/abe944)
- Salim, S., Lee, J. C., Janowiecki, S., et al. 2016, *ApJS*, 227, 2, doi: [10.3847/0067-0049/227/1/2](https://doi.org/10.3847/0067-0049/227/1/2)
- Sanders, D. B., & Mirabel, I. F. 1996, *ARA&A*, 34, 749, doi: [10.1146/annurev.astro.34.1.749](https://doi.org/10.1146/annurev.astro.34.1.749)
- Saunders, W., Sutherland, W. J., Maddox, S. J., et al. 2000, *MNRAS*, 317, 55, doi: [10.1046/j.1365-8711.2000.03528.x](https://doi.org/10.1046/j.1365-8711.2000.03528.x)
- Skinner, C. J., Smith, H. A., Sturm, E., et al. 1997, *Nature*, 386, 472, doi: [10.1038/386472a0](https://doi.org/10.1038/386472a0)
- Suess, K. A., Darling, J., Haynes, M. P., & Giovanelli, R. 2016, *MNRAS*, 459, 220, doi: [10.1093/mnras/stw666](https://doi.org/10.1093/mnras/stw666)
- Toba, Y., Oyabu, S., Matsuhara, H., et al. 2014, *ApJ*, 788, 45, doi: [10.1088/0004-637X/788/1/45](https://doi.org/10.1088/0004-637X/788/1/45)
- Veilleux, S., Kim, D. C., & Sanders, D. B. 1999, *ApJ*, 522, 113, doi: [10.1086/307634](https://doi.org/10.1086/307634)
- Veilleux, S., Kim, D. C., Sanders, D. B., Mazzarella, J. M., & Soifer, B. T. 1995, *ApJS*, 98, 171, doi: [10.1086/192158](https://doi.org/10.1086/192158)
- Weedman, D. W., & Houck, J. R. 2008, *ApJ*, 686, 127, doi: [10.1086/591123](https://doi.org/10.1086/591123)
- Wiggins, B. K., Migenes, V., & Smidt, J. M. 2016, *ApJ*, 816, 55, doi: [10.3847/0004-637X/816/2/55](https://doi.org/10.3847/0004-637X/816/2/55)
- Willett, K. W. 2012, in *Cosmic Masers - from OH to H0*, ed. R. S. Booth, W. H. T. Vlemmings, & E. M. L. Humphreys, Vol. 287, 345–349, doi: [10.1017/S1743921312007284](https://doi.org/10.1017/S1743921312007284)
- Wright, E. L. 2006, *PASP*, 118, 1711, doi: [10.1086/510102](https://doi.org/10.1086/510102)
- Yun, M. S., Reddy, N. A., & Condon, J. J. 2001, *ApJ*, 554, 803, doi: [10.1086/323145](https://doi.org/10.1086/323145)
- Zhang, C.-P., Xu, J.-L., Wang, J., et al. 2022, *Research in Astronomy and Astrophysics*, 22, 025015, doi: [10.1088/1674-4527/ac3fd2](https://doi.org/10.1088/1674-4527/ac3fd2)
- Zhang, C.-P., Jiang, P., Zhu, M., et al. 2023, *Research in Astronomy and Astrophysics*, 23, 075016, doi: [10.1088/1674-4527/acd58e](https://doi.org/10.1088/1674-4527/acd58e)
- Zhang, C.-P., Zhu, M., Jiang, P., et al. 2024, *SCPMA*, 67, 219511, doi: [10.1007/s11433-023-2219-7](https://doi.org/10.1007/s11433-023-2219-7)

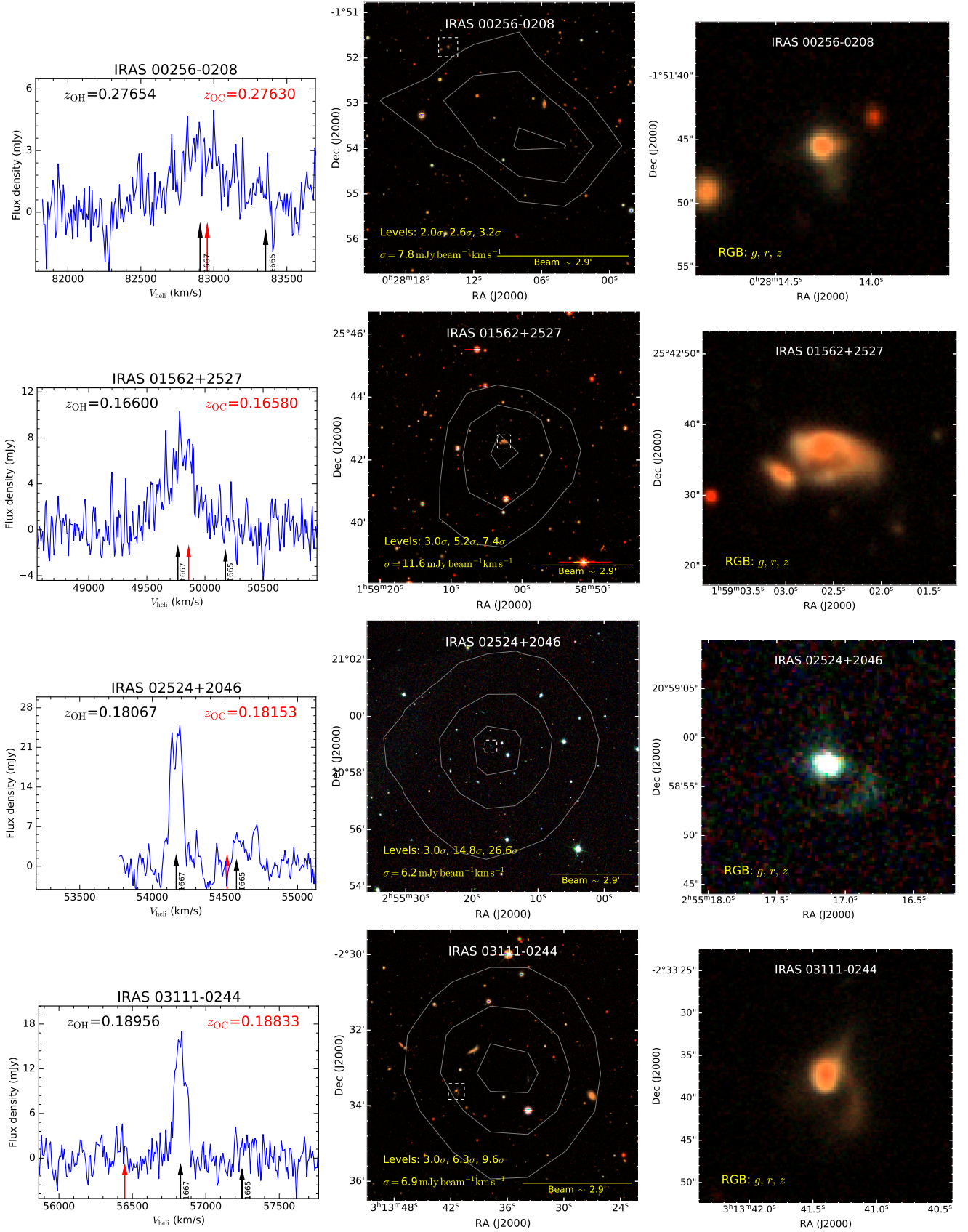


Figure 6. See caption in Figure 2

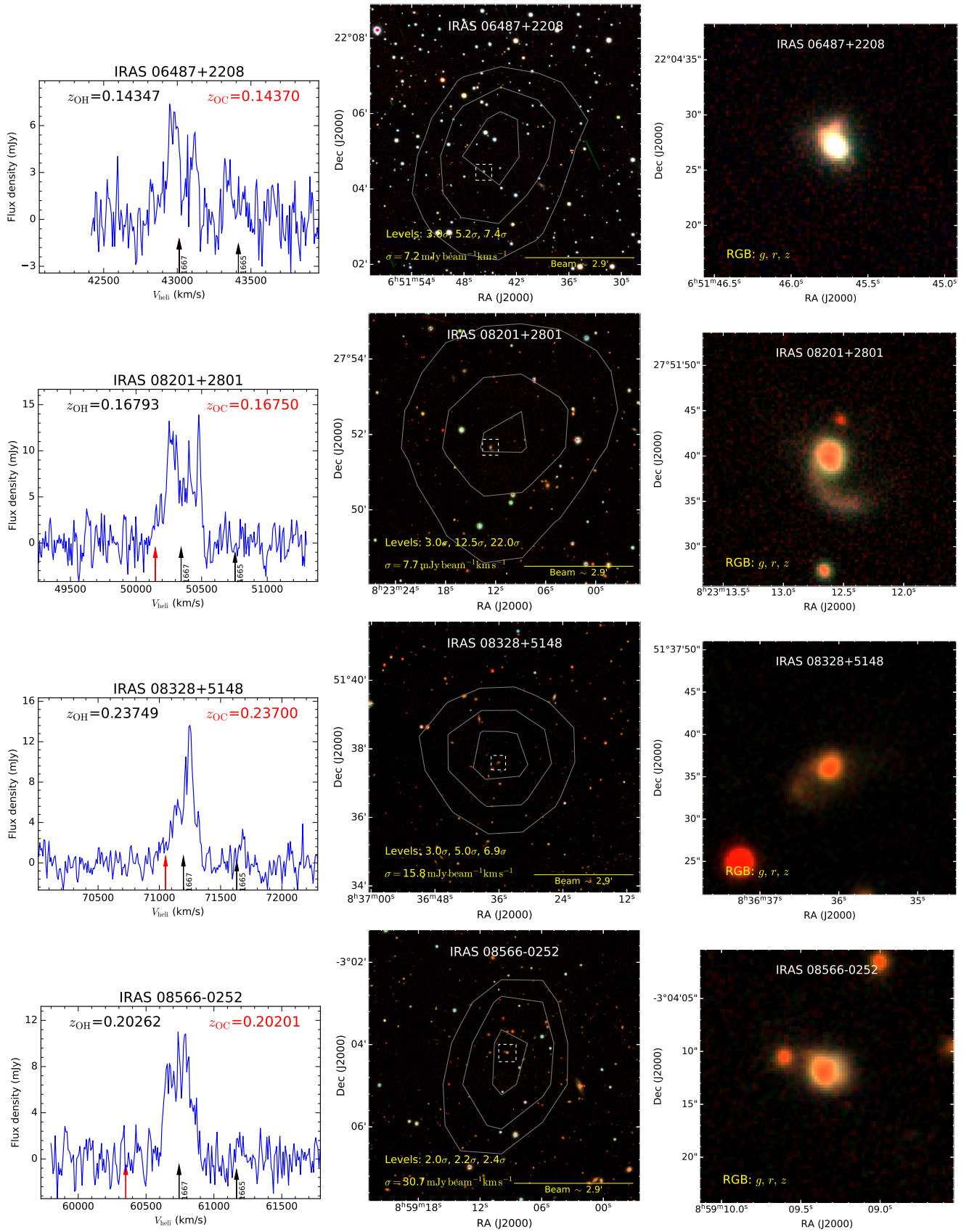


Figure 6 (Continued). See caption in Figure 2

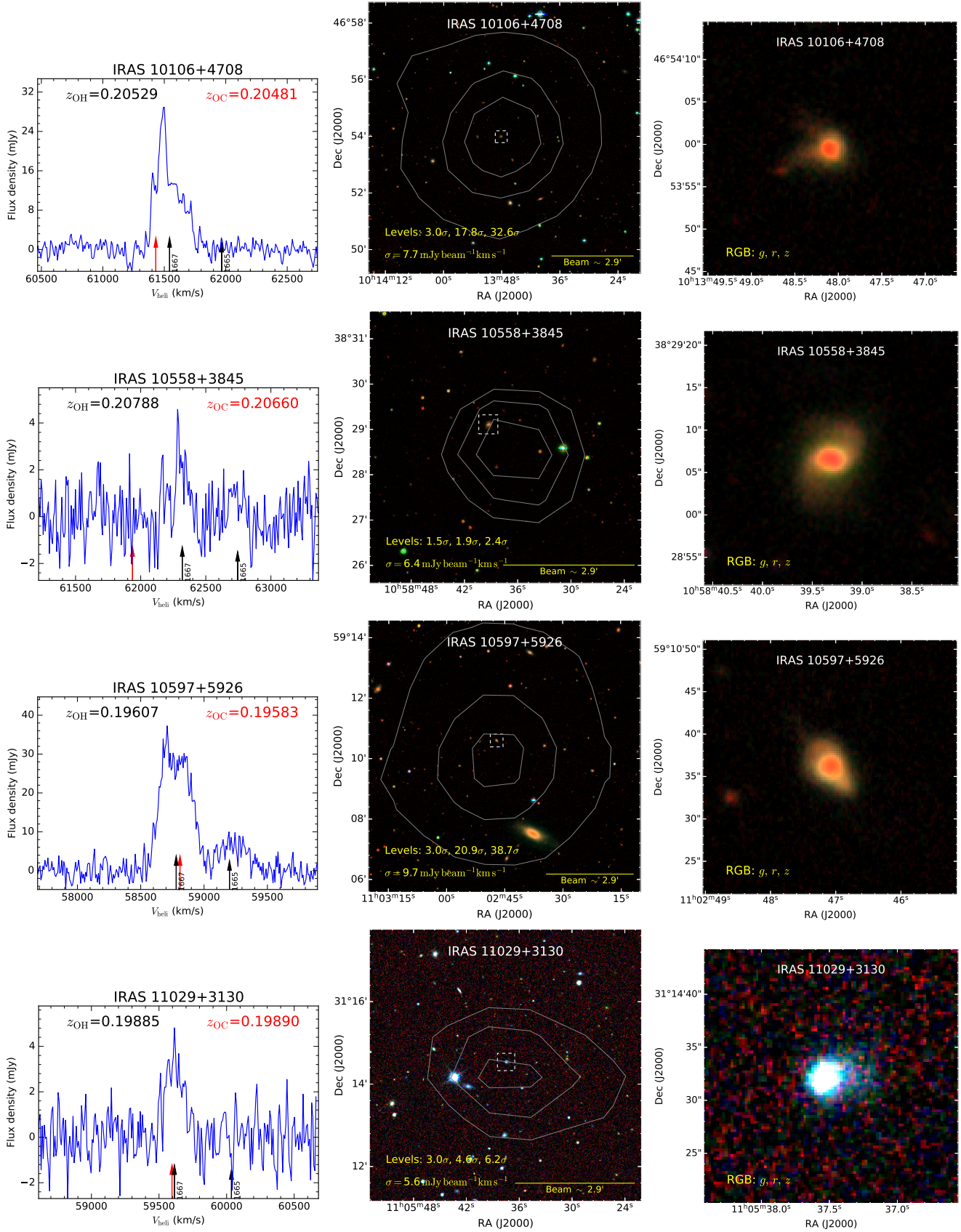


Figure 6 (Continued). See caption in Figure 2

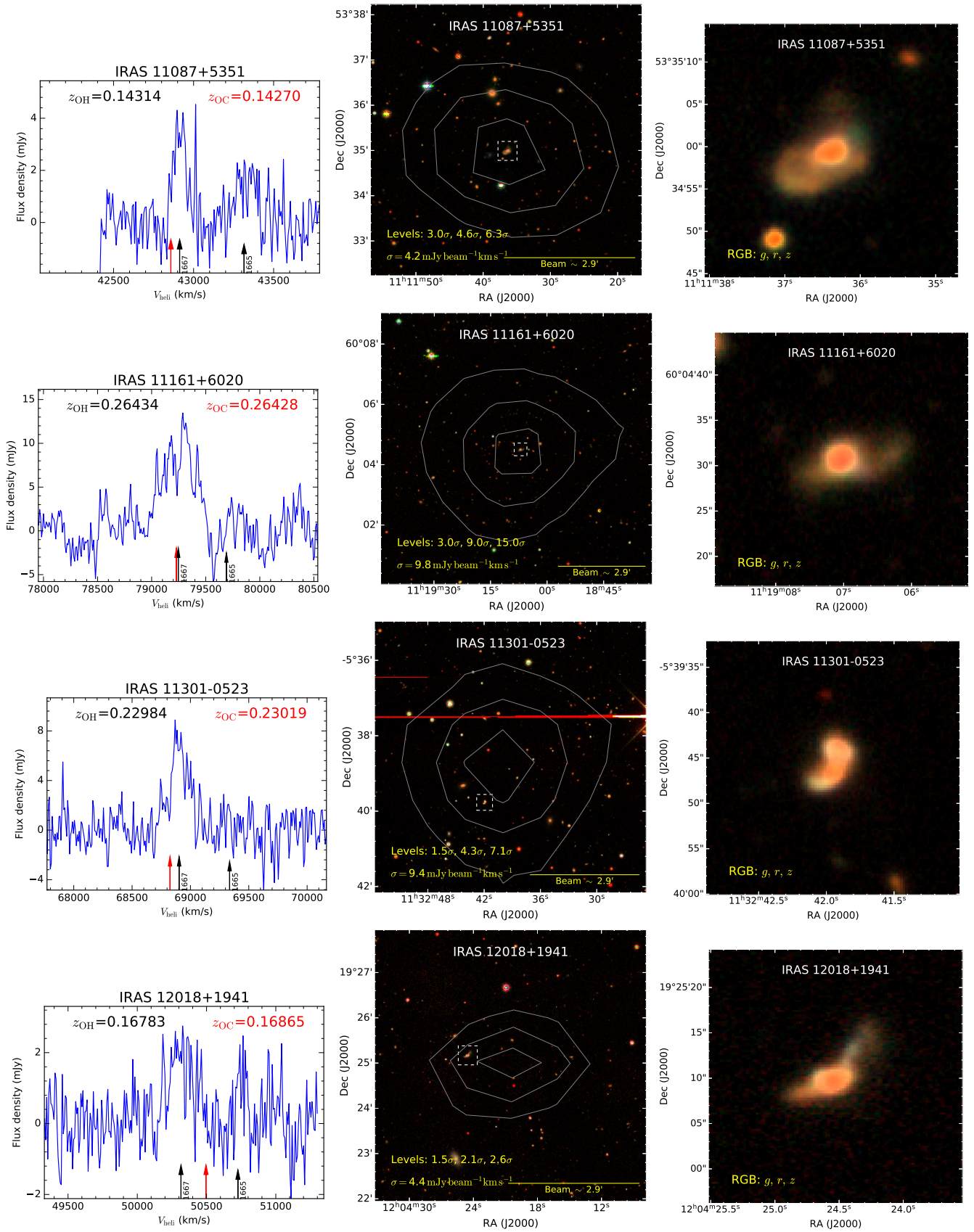


Figure 6 (Continued). See caption in Figure 2

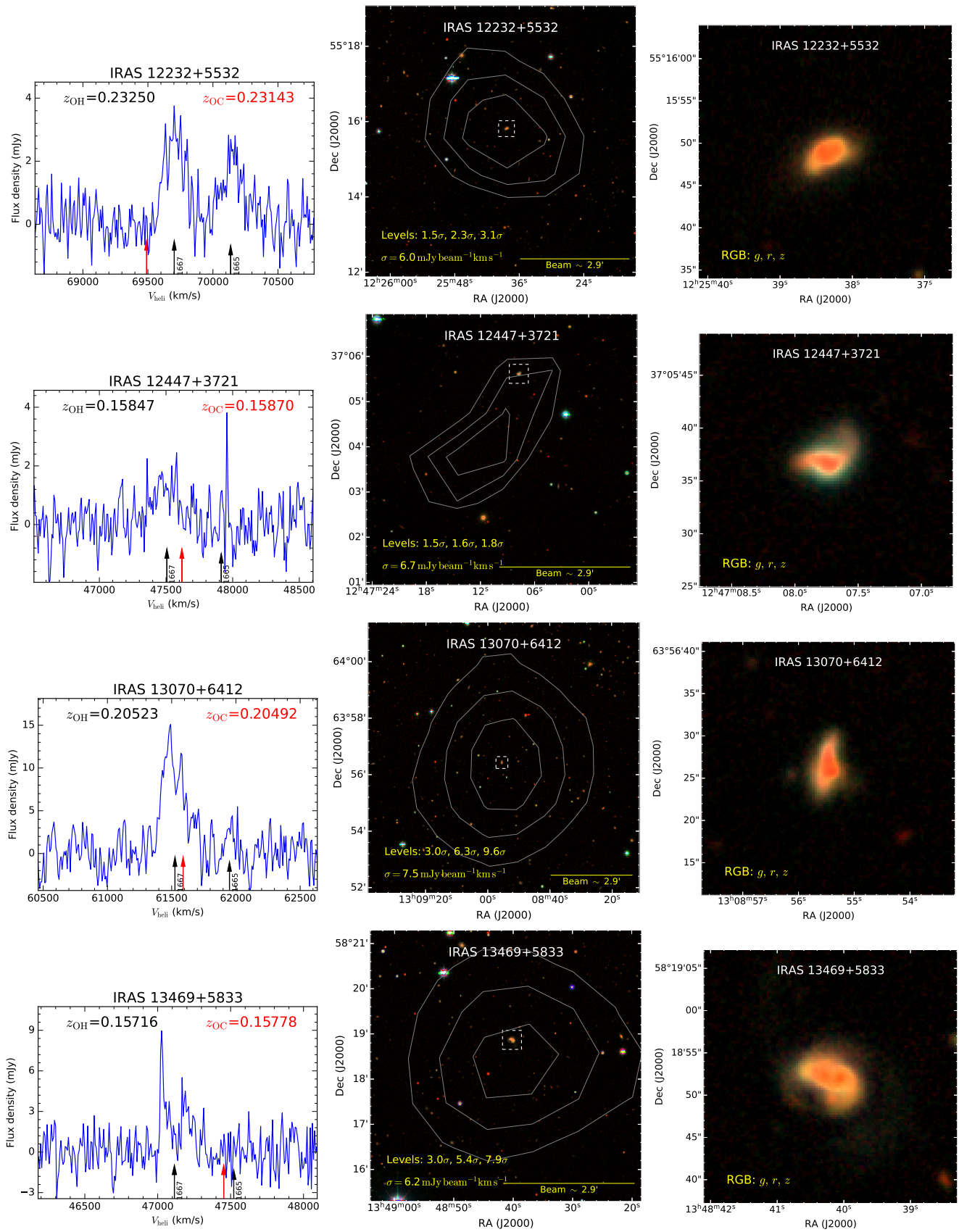


Figure 6 (Continued). See caption in Figure 2

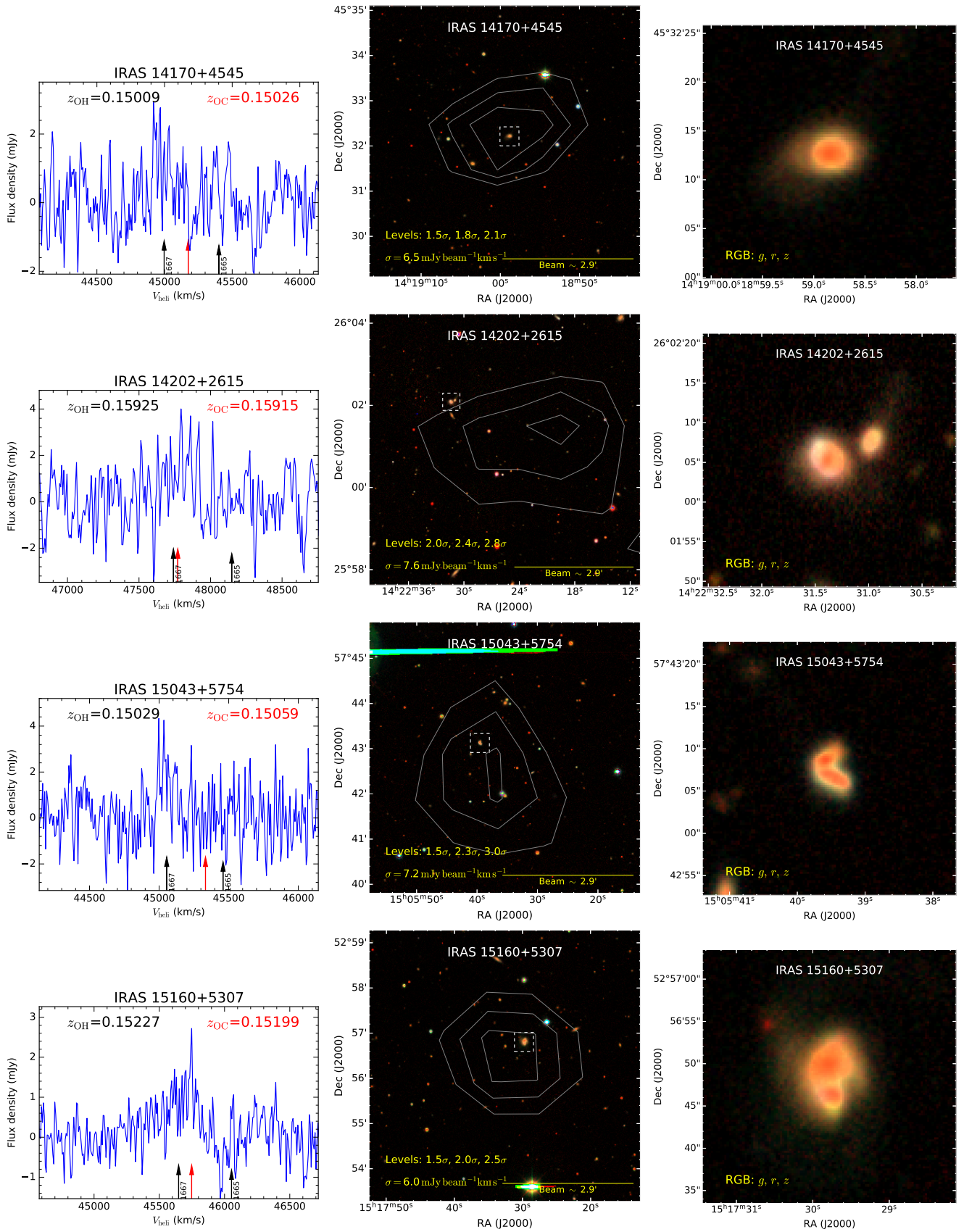


Figure 6 (Continued). See caption in Figure 2

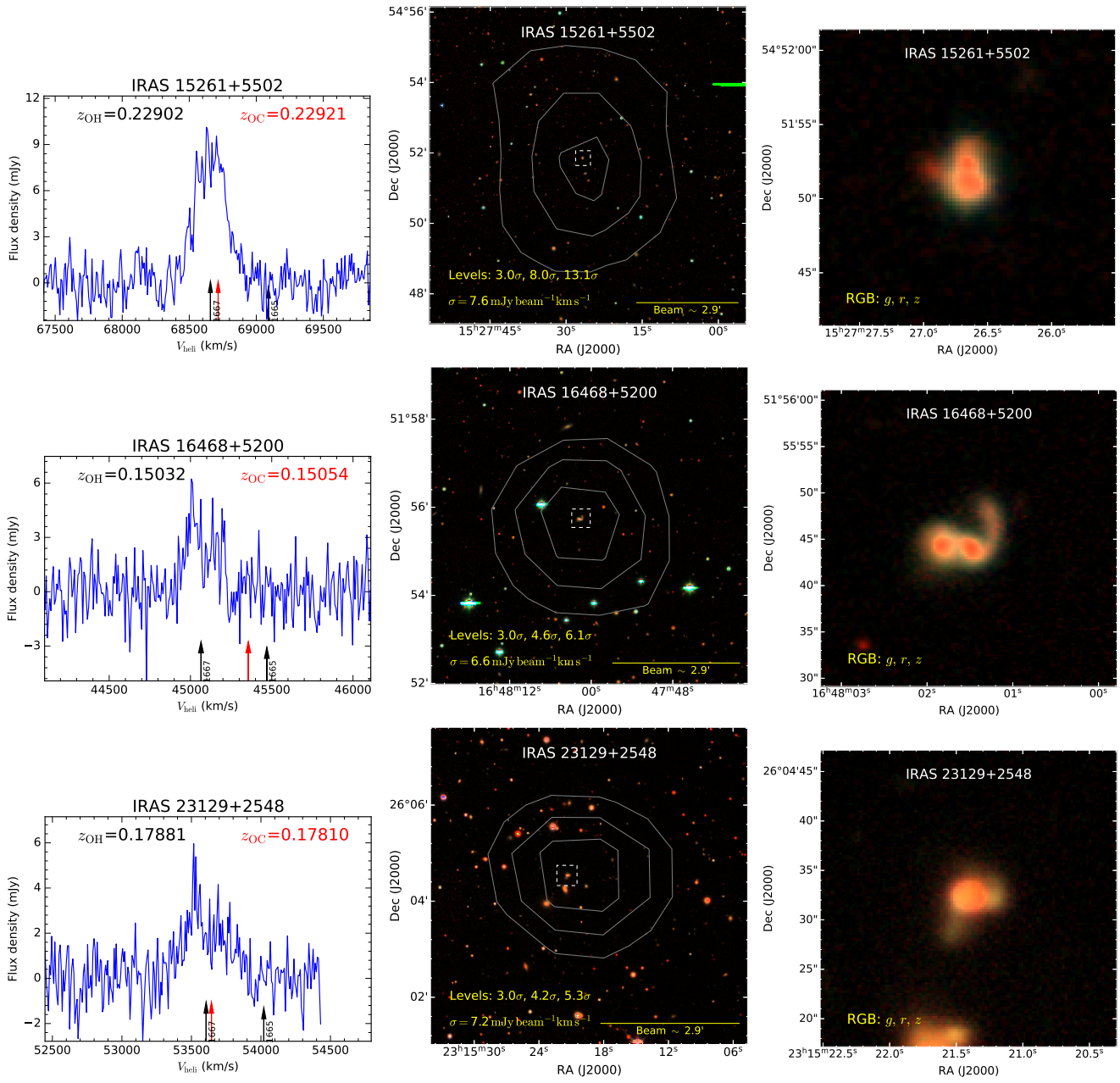


Figure 6 (Continued). See caption in Figure 2